


Quantum proton entanglement on a nanocrystalline silicon surfaceTakahiro Matsumoto^{1,2,*}, Hidehiko Sugimoto^{3,†}, Takashi Ohhara⁴, Akio Tokumitsu,⁵
Makoto Tomita,⁶ and Susumu Ikeda⁷¹*Graduate School of Design and Architecture, Nagoya City University, Nagoya 464-0083, Japan*²*Graduate School of Medical Sciences, Nagoya City University, Nagoya 464-0083, Japan*³*Department of Physics, Faculty of Science and Engineering, Chuo University, Tokyo 112-8551, Japan*⁴*Neutron Science Section, J-PARC Center, Japan Atomic Energy Agency, Ibaraki 319-1195, Japan*⁵*Graduate School of Science, Nagoya City University, Nagoya 467-8501, Japan*⁶*Department of Physics, Faculty of Science, Shizuoka University, Shizuoka 422-8529, Japan*⁷*High Energy Accelerator Research Organization, Ibaraki 319-1195, Japan* (Received 28 September 2020; revised 28 February 2021; accepted 28 April 2021; published 1 June 2021)

We investigate the quantum entangled state of two protons terminating on a silicon surface. The entangled states were detected using the surface vibrational dynamics of nanocrystalline silicon with inelastic neutron scattering spectroscopy. The protons are identical, therefore the harmonic oscillator parity constrains the spin degrees of freedom, forming strongly entangled states for all the energy levels of surface vibrations. Compared to the proton entanglement previously observed in hydrogen molecules, this entanglement is characterized by an enormous energy difference of 113 meV between the spin singlet ground state and the spin triplet excited state. We theoretically demonstrate the cascade transition of terahertz entangled photon pairs utilizing proton entanglement. A combination of proton qubits and a modern silicon technology can result in a natural unification of computing platforms, thereby achieving unprecedented levels of massive parallelism processing.

DOI: [10.1103/PhysRevB.103.245401](https://doi.org/10.1103/PhysRevB.103.245401)**I. INTRODUCTION**

Entangled states represent one of the most dramatic conceptual changes when transitioning from classical to quantum physics [1–3]. To date, many approaches have been adopted to create entangled states, such as utilizing superconducting states [4–7], atomic ion traps [8–11], electrons and/or holes in semiconductors [12–15], molecular spins [16–18], and nitrogen-vacancy centers in diamond [19–21]. However, these methods present several engineering challenges, such as limitations in the fabrication of a large number of qubits, the requirement of maintaining ultralow temperatures below 1 K, or the necessity to use chemically and isotopically ultrapurified materials.

The utilization of surfaces or interfaces can yield useful functionalities for the above quantum technologies such as scalability, transduction, and networking. In particular, the use of surfaces is inevitable for nanomechanical resonators [22–24], high spatial resolution sensing [25,26], as well as atom- and ion-chip traps and superconducting qubits. However, owing to the existence of unpaired electron spins on the surface of the host material, they generally suffer from decoherence [27–29]. Therefore, to obtain stable coherent qubits, it is necessary to determine the spin states of surface atoms. The most powerful technique for investigating spin states is inelastic neutron scattering (INS).

Herein, we show that measurements of the scattering function via INS spectroscopy help us determine the vibrational dynamics of two protons terminating on the surface (SiH₂ surface) of nanocrystalline silicon (n-Si). We present evidence of the quantum entangled states of the two protons. These entangled states are characterized by an anomalous coherent scattering process with an incoherent scattering cross section. This evidence is shown by an interference pattern in the scattering spectra at the odd number (n_{odd}) energy levels of SiH₂ scissor (SC) modes, whereas normal coherent scattering occurs at the even number (n_{even}) energy levels of the modes. These features are lost when the indistinguishability is broken by partially substituting protons with deuterons.

A crucial aspect of this research is that the protons are identical, and the harmonic oscillator parity constrains the spin degrees of freedom. This constraint leads to the formation of strongly entangled states for all the energy levels of SiH₂ vibrations. Furthermore, compared to the previously reported proton entanglement (hydrogen molecule) [30,31], this entanglement is characterized by a significantly larger energy difference of 113 meV between the spin singlet ground energy level ($n = 0$) and the spin triplet excited energy level ($n = 1$). We briefly discuss a theoretical demonstration of the cascade transitions of terahertz (THz) entangled photon pairs utilizing proton entanglement. These solid-state entangled proton qubits atomically arranged on the surface of Si could result in a natural unification of computing platforms, thereby achieving unprecedented levels of storing, processing, and transferring technologies.

*Corresponding author: matsumoto@sda.nagoya-cu.ac.jp†Corresponding author: sugimoto.hidehiko@gmail.com

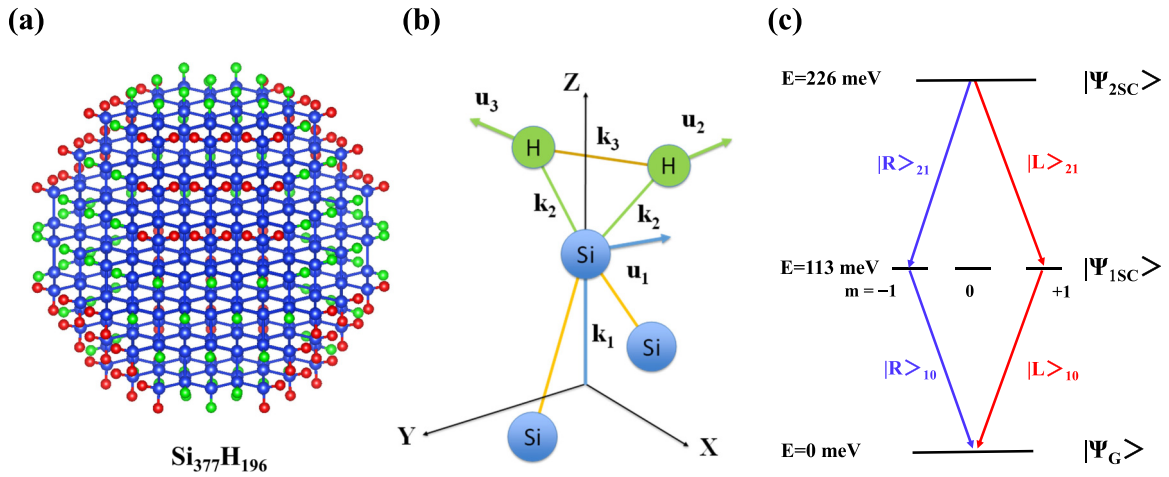


FIG. 1. (a) Schematic of n-Si composed of 377 Si atoms (blue balls) and 196 H atoms, with a diameter of 2.4 nm. The n-Si surface consists of SiH (green balls) or SiH_2 terminations (red balls). The ratio of SiH_2 to SiH terminations is modeled as 1:1 to coincide with the Fourier-transform infrared spectrum measurements. (b) Schematic to analyze SiH_2 vibration dynamics. The position of each atom (Si : \mathbf{r}_1 , H : \mathbf{r}_2 , and H : \mathbf{r}_3) is expressed by introducing the displacement vectors \mathbf{u}_1 , \mathbf{u}_2 , and \mathbf{u}_3 from the equilibrium positions \mathbf{R}_1 , \mathbf{R}_2 , and \mathbf{R}_3 as $\mathbf{r}_1 = \mathbf{u}_1 + \mathbf{R}_1$, $\mathbf{r}_2 = \mathbf{u}_2 + \mathbf{R}_2$, and $\mathbf{r}_3 = \mathbf{u}_3 + \mathbf{R}_3$. The force constants of Si-Si and Si-H bonds and H-H interactions are expressed as \mathbf{k}_1 , \mathbf{k}_2 , and \mathbf{k}_3 , respectively. (c) Entanglement energy levels using scissor modes. The evenly spaced energy levels have wave functions (Ψ) composed of the product of the harmonic oscillator and proton spin. For $E = 0$ and 226 meV, the scissor modes have spin singlet states (angular momentum $J = 0$), and for $E = 113$ meV the scissor mode has spin triplet states ($J = 1, m = -1, 0, +1$). A cascade transition of 27-THz entangled photon pairs can be achieved utilizing the scissor modes. Here, $|R_{n-1}\rangle$ (blue arrow) and $|L_{n-1}\rangle$ (red arrow) denote the transition from the $n - 1$ level with right and left circulation polarization, respectively.

II. EXPERIMENT AND RESULTS

INS measurements were performed on a time-of-flight MARI chopper spectrometer at the ISIS Facility at the Rutherford Appleton Laboratory. We measured the contour plots of the dynamic structure factor $S(Q, \hbar\omega)$ [scattering intensity (S), energy ($\hbar\omega$), and momentum-transfer (Q) axis] for n-Si at 50 K with an incident neutron energy $E_i = 0.3$ eV. For the INS measurements, 1 g of powdered n-Si was used to fabricate samples by electrochemical anodization [32–34]; they were wrapped in aluminum foil and rolled into a cylindrical shape to minimize the extinction effect. For powdered n-Si, pure proton (100%: n-Si:H), or a mix of deuterium and proton (85% and 15%, respectively) terminated samples (n-Si : $\text{H}_{0.15}\text{D}_{0.85}$) were fabricated using electrochemical anodization. Isotope substitution of the termination was performed by mixing the proton and deuterium electrolyte [33]. The isotope concentration was selected such that the H-Si-D vibrational modes were observed, whereas the H-Si-H vibrational modes were not observed in $S(Q, \hbar\omega)$. The diameter of both the n-Si:H and n-Si : $\text{H}_{0.15}\text{D}_{0.85}$ is in the range 0.8–5 nm, with an average diameter of approximately 2.4 nm [34–36].

Figure 1(a) shows the schematic of n-Si composed of 377 Si atoms and 196 H atoms, with a diameter of 2.4 nm. The surface of n-Si is composed of approximately 50% SiH (green balls) and 50% SiH_2 terminations (red balls). Previous studies on the Fourier-transform infrared spectrum measurements for n-Si obtained a similar ratio (SiH : $\text{SiH}_2 = 1 : 1$) for surface terminations [36,37]. Herein, we focused on the vibrational dynamics of SiH_2 , as shown in Fig. 1(b), as two-proton entanglement was clearly observed in the vibrational modes [38,39] of SiH_2 . As an example of the entanglement states,

the energy level diagram, vibrational wave functions, and spin states of the SC modes are schematically summarized in Fig. 1(c).

Figure 2 shows the INS data of n-Si. Figure 2(a) shows the contour plot of $S(Q, \hbar\omega)$ for $\hbar\omega$ in the range 90–140 meV and the momentum transfer (Q) in the range 3–15 \AA^{-1} . The figure shows a series of vibrational levels, which represent the first ($1N = 81$ meV) and second ($2M = 138$ meV) excited SiH bending modes [38], and the 1SC mode (1SC = 113 meV) [38,39]. The 1SC mode was sliced at 113 meV with a sliced energy width of 5 meV. $S(Q, \hbar\omega_{SC} = 113 \text{ meV})$ has a spectral peak at $Q = 6.8 \text{ \AA}^{-1}$ and exhibits a clear interference pattern, indicated by solid red circles in Fig. 2(c). The plot of the Fourier-transformation (FT) of the sliced $S(Q, \hbar\omega_{SC} = 113 \text{ meV})$ is indicated by red circles in Fig. 2(d), which show a clear spectral peak at 2.5 \AA . This FT spectral peak at 2.5 \AA suggests a strong correlation between the protons of H-Si-H species. We can consider various structures for the 1×1 (100):H terminated surface such as a symmetric or a canted dihydride structure [40]. The evidence that the SC vibrational modes are described by the harmonic oscillator without anharmonicity (described in Analysis section) suggests that the vibrational dynamics is free from surrounding hydrogen interaction, and thus we consider that almost all the structure of H-Si-H species takes the canted dihydride form.

Contrary to the 1SC mode, the 2SC mode, which occurs between the third excited $3M$ (217 meV) and $3N$ (237 meV) bending modes [38], is nearly undetectable among the background scattering, as shown in the $S(Q, \hbar\omega)$ of Fig. 2(b). This disappearance is clearly displayed by the sliced $S(Q, 2\hbar\omega_{SC} = 226 \text{ meV})$ plot, indicated by solid blue circles in Fig. 2(c).

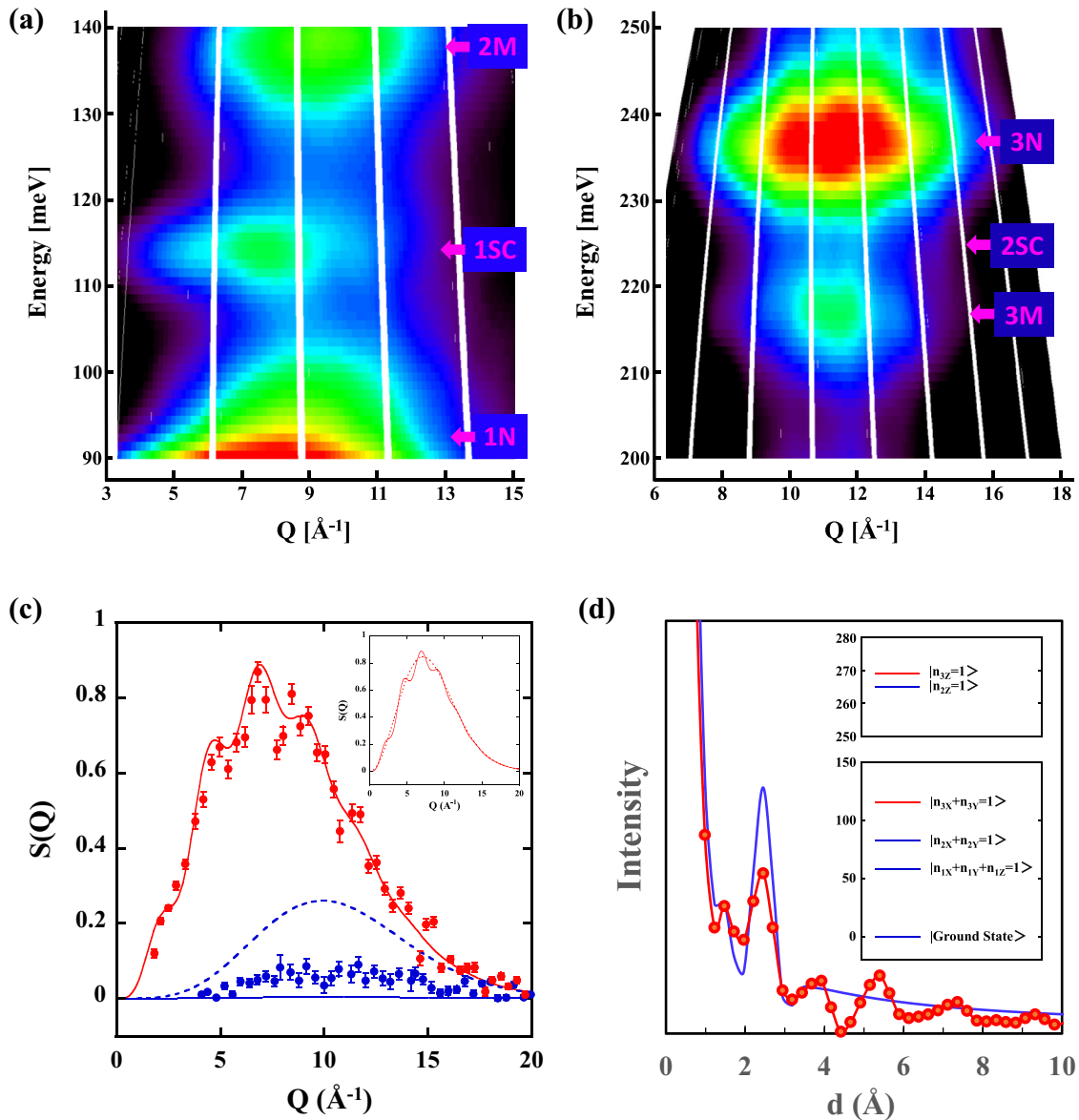


FIG. 2. Two-dimensional $S(Q, \hbar\omega)$ plots of (a) 1SC (113 meV) and (b) 2SC (226 meV) modes. (c) Sliced $S(Q)$ spectrum of 1SC mode (red circles) and 2SC mode (blue circles) derived from the two-dimensional $S(Q, \hbar\omega)$ plots. The red and blue lines are theoretically fitted $S(Q)$ curves with the effects from proton entanglement for 1SC and 2SC modes. The dotted red (inset) and blue lines are theoretically calculated $S(Q)$ curves without the entanglement effect (distinguishable case) for comparison. (d) FT spectra of both sliced (red circles) and theoretically fitted (blue line) $S(Q)$ for the 1SC mode. Inset shows the first excited energy states of SiH_2 vibrations. Here the red or blue lines represent triplet or singlet states, and $E(n_{1X} + n_{1Y} + n_{1Z} = 1) = 58$ meV, $E(n_{2X} + n_{2Y} = 1) = 82$ meV, $E(n_{3X} + n_{3Y} = 1) = 113$ meV, $E(n_{2Z} = 1) = 265$ meV, and $E(n_{3Z} = 1) = 269$ meV.

When the INS data of $n\text{-Si} : \text{H}_{0.15}\text{D}_{0.85}$ was measured, the corresponding isotopically shifted SC mode (1DSC; 97 meV [33]), shown in the $S(Q, \hbar\omega)$ of Fig. 3(a), did not exhibit the interference pattern in the sliced $S(Q, \hbar\omega_{\text{DSC}} = 97$ meV). Both the sliced $S(Q, \hbar\omega_{\text{DSC}} = 97$ meV) and FT spectra, plotted as red circles in Figs. 3(c) and 3(d), indicate the disappearance of the interference. Additionally, the $S(Q, \hbar\omega)$ of the 2DSC mode ($2\hbar\omega_{\text{DSC}} = 194$ meV) exhibits intense scattering, whose intensity is approximately 60% that of the second excited $2N$ bending mode ($2N = 159$ meV) [38], as shown in Fig. 3(b). This is clearly exhibited by the sliced $S(Q, 2\hbar\omega_{\text{DSC}} = 194$ meV), plotted as solid blue circles in Fig. 3(c). Here, we note that the scattering cross section of the

protons in the INS measurements is over ten times larger than that of the deuterons ($\sigma_{\text{scatt}}^{(\text{D})}/\sigma_{\text{scatt}}^{(\text{H})} \approx 7.64/82.03$ [41]), therefore the $S(Q, \hbar\omega)$ obtained here predominantly originates from the protons, despite the lower proton concentration.

These results can be summarized as follows: for the SC modes, (a) the intense scattering exhibits an interference pattern at the n_{odd} energy levels (Fig. 2), (b) the scattering spectra at the n_{even} energy levels are not detectable (Fig. 2), and (c) these features disappear when the indistinguishability is broken by partially substituting protons with deuterons (Fig. 3). These results provide direct evidence that the vibrational and proton spin wave functions are correlated owing to the indistinguishability of the two protons. This correlation forms

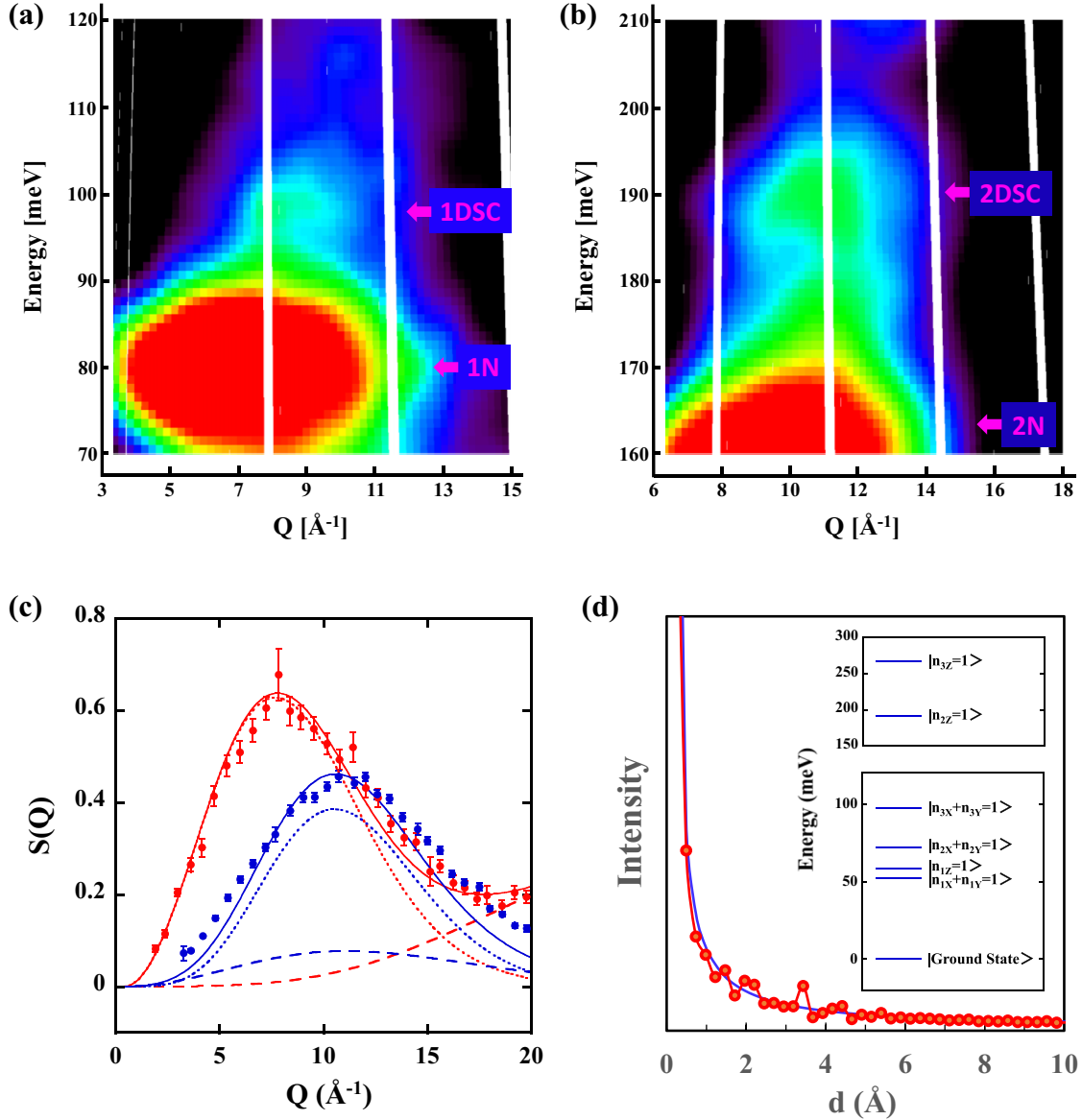


FIG. 3. Two-dimensional $S(Q, \hbar\omega)$ plots of (a) 1DSC (97 meV) and (b) 2DSC (194 meV) modes. (c) Sliced $S(Q)$ spectrum of 1DSC mode (red circles) and 2DSC mode (blue circles) derived from the two-dimensional $S(Q, \hbar\omega)$ plots. The red and blue lines are theoretically fitted $S(Q)$ curves consisting of both the distinguishable case (dotted red or blue line) and other scattering components (broken blue line: Si-D stretching). (d) FT spectra of both sliced (red circles) and theoretically fitted (blue line) $S(Q)$ for the 1DSC mode. The peak at 2.5 \AA disappeared owing to loss of the proton entanglement effect. Inset shows the first excited energy states of SiHD vibrations, where $E(n_{1X} + n_{1Y} = 1) = 52 \text{ meV}$, $E(n_{1Z} = 1) = 58 \text{ meV}$, $E(n_{2X} + n_{2Y} = 1) = 72 \text{ meV}$, $E(n_{3X} + n_{3Y} = 1) = 97 \text{ meV}$, $E(n_{2Z} = 1) = 192 \text{ meV}$, and $E(n_{3Z} = 1) = 267 \text{ meV}$.

strongly entangled states between the spin triplet for the n_{odd} energy levels and the spin singlet for the n_{even} energy levels in a harmonic potential, as shown in Fig. 1(c). In particular, the experimental results indicating an almost undetectable scattering intensity for the 2SC mode and a considerably enhanced scattering intensity for the 2DSC mode are direct evidence that a mixture of singlet and triplet spin states does not occur and the 2SC mode only has a spin singlet state. (The ground state has a spin singlet state, and the scattering from the ground state to the 2SC state is dominated by a spin nonflip process.)

III. ANALYSIS

Here, we analyze the two-proton dynamics in coordination with the Si motion. The model shown in Fig. 1(b) represents lateral vibrations in the X-Y plane and longitudinal vibrations along the Z axis. The position of each atom ($\text{Si}^{(1)} : \mathbf{r}_1, \text{H}^{(2)} : \mathbf{r}_2, \text{H}^{(3)} : \mathbf{r}_3$) can be expressed by introducing the displacement vectors $\mathbf{u}_1, \mathbf{u}_2$, and \mathbf{u}_3 from the equilibrium positions $\mathbf{R}_1, \mathbf{R}_2$, and \mathbf{R}_3 , as follows: $\mathbf{r}_1 = \mathbf{u}_1 + \mathbf{R}_1$, $\mathbf{r}_2 = \mathbf{u}_2 + \mathbf{R}_2$, and $\mathbf{r}_3 = \mathbf{u}_3 + \mathbf{R}_3$, where the superscript 1 indicates $\text{Si}^{(1)}$, and the superscripts 2 and 3 indicate $\text{H}^{(2)}$ and $\text{H}^{(3)}$, respectively. In this model, the Schrödinger equation can

be written as

$$\sum_{v=1}^3 \sum_{\rho=X}^Z \left(-\frac{\hbar^2}{2} \frac{\partial^2 \Phi}{\partial \xi_{v\rho}^2} + \frac{1}{2} \omega_{v\rho}^2 \xi_{v\rho}^2 \Phi \right) = E \Phi, \quad (1)$$

where $\Phi = \prod_{v=1}^3 \prod_{\rho=X}^Z \phi_{n_{v\rho}}(\xi_{v\rho})$ ($\phi_{n_{v\rho}}(\xi_{v\rho})$ is the harmonic oscillator wave function), $\omega_{v\rho}$ is the eigenvalue frequencies depending on the force constants ($k_{1\rho}, k_{2\rho}, k_{3\rho}$) and the masses of Si (μ_1) or H (μ_2), E is the energy eigenvalue, and ρ denotes the $X, Y,$ or Z coordinates. Here, $\xi_{v\rho}$ is the normal coordinate described with the displacement vectors as

$$\xi_{1\rho} = \frac{1}{\sqrt{\gamma_\rho^2 + 1}} \left\{ \sqrt{\mu_1} u_{1\rho} + \frac{\gamma_\rho}{\sqrt{2}} (\sqrt{\mu_2} u_{2\rho} + \sqrt{\mu_3} u_{3\rho}) \right\}, \quad (2)$$

$$\xi_{2\rho} = \frac{1}{\sqrt{\gamma_\rho^2 + 1}} \left\{ -\gamma_\rho \sqrt{\mu_1} u_{1\rho} + \frac{1}{\sqrt{2}} (\sqrt{\mu_2} u_{2\rho} + \sqrt{\mu_3} u_{3\rho}) \right\}, \quad (3)$$

$$\xi_{3\rho} = \frac{1}{\sqrt{2}} (\sqrt{\mu_2} u_{2\rho} - \sqrt{\mu_3} u_{3\rho}), \quad (4)$$

where γ_ρ is the parameter determined by both the force constants and the masses [38] in order to reproduce the experimentally observed vibrational frequencies. We note here that when $\mu_2 = \mu_3$, the normal coordinates in Eqs. (2)–(4) can be separated into the two symmetrical parts ($\xi_{1\rho}, \xi_{2\rho}$), and one antisymmetrical part ($\xi_{3\rho}$) for the exchange of proton coordinates ($u_{2\rho} \leftrightarrow u_{3\rho}$). The wave function at the state λ (initial or final), $|\Psi_\lambda\rangle$, is described by the product of the vibrational state $|\Phi_\lambda\rangle$ described by the harmonic oscillators and the spin state of nuclei $|\sigma_\lambda\rangle$ as $|\Psi_\lambda\rangle = |\Phi_\lambda\rangle \otimes |\sigma_\lambda\rangle$. Here we note that the spin of Si is 0 [41], therefore the scattering of neutron is affected by the spins of protons.

Finally, the scattering matrix elements $S(Q, \hbar\omega)$ can be described as

$$S(Q, \hbar\omega) = \sum_i \sum_f \sum_{\alpha=1}^3 \sum_{\beta=1}^3 p_i b_{\alpha\beta}^{(fi)} \langle \Phi_i | \exp(i\mathbf{Q} \cdot \mathbf{r}_\alpha) | \Phi_f \rangle^* \times \langle \Phi_f | \exp(i\mathbf{Q} \cdot \mathbf{r}_\beta) | \Phi_i \rangle \delta(\hbar\omega - E_f + E_i), \quad (5)$$

where the subscripts i and f represent the initial and final state, respectively; p_i is the statistical weight; \mathbf{r}_α is the position vector of nucleus α ; and $b_{\alpha\beta}^{(fi)}$ is the scattering coefficient calculated from the nuclear spin wave functions $|\sigma_\lambda\rangle$ for each nucleus ($\alpha, \beta = 1$ for Si and 2, 3 for H) [42–44].

The proton is a spin 1/2 fermion and two protons should form an antisymmetric wave function to facilitate the exchange of their coordinates. When we apply parity operator P_{23} to the normal coordinates shown in Eqs. (2)–(4), where P_{23} exchange between proton 2 and 3 coordinates, we obtain $P_{23}\xi_{1\rho} = \xi_{1\rho}$, $P_{23}\xi_{2\rho} = \xi_{2\rho}$ and $P_{23}\xi_{3\rho} = -\xi_{3\rho}$. In this case, the harmonic oscillators that contain the $n_{3\rho} = n_{\text{odd}}$ energy levels of the SC mode have the following antisymmetry: $P_{23}\Phi_{n_{\text{odd}}} = -\Phi_{n_{\text{odd}}}$. This antisymmetry entails symmetrical triplet nuclear spin states. For all other energy levels except $n_{3\rho} = n_{\text{odd}}$, such as $n = n_{1\rho}, n_{2\rho}$, and $n_{3\rho} = n_{\text{even}}$ levels, the harmonic oscillators have the following symmetry: $P_{23}\Phi_n =$

Φ_n . This symmetry entails antisymmetrical singlet nuclear spin states. The calculated energy levels and the spin states for the first excited states are summarized in the inset of Fig. 2(d), where the red line or blue line represents triplet states or singlet states with the energy levels of $E(n_{1X} + n_{1Y} + n_{1Z} = 1) = 58$ meV, $E(n_{2X} + n_{2Y} = 1) = 82$ meV, $E(n_{3X} + n_{3Y} = 1) = 113$ meV, $E(n_{2Z} = 1) = 265$ meV, and $E(n_{3Z} = 1) = 269$ meV.

The energy difference between the singlet ground state and the triplet excited state is 113 meV, which is enormous compared to that observed in hydrogen molecules (approximately 10 meV between ortho- and parahydrogen states [30,31]). The transition from the triplet excited state to the singlet ground state is forbidden by the spin orthogonality. In this case, the transition from the 1SC state to the ground state is possible by the magnetic dipole interactions. The lifetime of this state seems to be very long and our analysis shows that the lifetime is more than 1 ms. Although the experimental evaluation of the transition matrix element of the electromagnetic interaction is necessary, we consider that this feature is promising for the generation of population inversion, induced THz radiation by magnetic dipole interaction [45–47], qubits operations, and/or quantum memories.

The calculated results of the $b_{\alpha\beta}^{(fi)}$ coefficients in Eq. (5) for the 1SC level are presented in Table I, singlet to triplet. The $b_{\alpha\beta}^{(fi)}$ coefficients for the 2SC level are also presented in Table I, singlet to singlet. One particularly interesting point from the analysis was the difference of the magnitude of the cross terms such as $b_{23}^{(fi)}$ and $b_{32}^{(fi)}$ at the 1SC or 2SC level. For the scattering from the 1SC level, the coherent scattering occurs between two protons with 2.5 Å distance, however its scattering cross sections, especially the diagonal terms as well as the cross terms, are described by the incoherent scattering cross section $\sigma_{\text{inc}}^{(\text{H})}$ [42–44]. On the other hand, for the scattering from the 2SC level, the coherent scattering occurs between two protons, and the scattering is described by the non-spin-flip coherent process as shown in Table I, singlet to singlet [42–44]. Therefore the scattering intensity as well as the amplitude of the interference in the 2SC level are small to be observed.

The solid red line in Fig. 2(c) and the solid blue line in Fig. 2(d) show the theoretically calculated $S(Q, \hbar\omega = 113$ meV) and the FT spectrum, respectively, including the effects of proton entanglement. A powder average operation [38,48,49], which represents the averaging of the absolute square of the transition matrix elements over the solid angle between Q and the displacement vector of each nucleus, was performed to obtain these theoretical curves. The interference behavior of the spectrum was reproduced and the theoretical curves accurately fit the experimental results. The peak at 2.5 Å in the FT spectra represents the distance between two protons, which was confirmed theoretically. For comparison, we also plotted the theoretical $S(Q, \hbar\omega = 113$ meV), without the effects from entanglement, as the dotted red line in the inset of Fig. 2(c). Here, the coefficient $b_{\alpha\beta}^{(fi)}$ was selected based on Table I, distinguishable case, where we replace $\sigma_{\text{scatt}}^{(\text{D})}$ to $\sigma_{\text{scatt}}^{(\text{H})}$ and $(\sigma_{\text{coh}}^{(\text{D})})^{1/2}$ to $-(\sigma_{\text{coh}}^{(\text{H})})^{1/2}$. Without the entanglement, the interference disappeared owing to the negligible size of the off-diagonal coefficient

TABLE I. Relation between scattering coefficients $b_{\alpha\beta}^{(fi)}$ (1: Si, 2: H, and 3: H) and cross sections (σ_{inc} : incoherent, σ_{coh} : coherent, σ_{scatt} : coherent + incoherent) used in Eq. (5). The two matrices of singlet to triplet and singlet to singlet are for calculating $S(Q, \hbar\omega)$ from the singlet ground state to the triplet excited state (1SC mode), and the singlet ground state to the singlet excited states (2SC mode). The matrix without the effect of entanglement is denoted as the distinguishable case (1: Si, 2: H, and 3: D).

	$\beta = 1$	$\beta = 2$	$\beta = 3$
$b_{\alpha\beta}^{(fi)}$ Singlet-Triplet			
$\alpha = 1$	0	0	0
$\alpha = 2$	0	$\sigma_{\text{inc}}^{(\text{H})}$	$-\sigma_{\text{inc}}^{(\text{H})}$
$\alpha = 3$	0	$-\sigma_{\text{inc}}^{(\text{H})}$	$\sigma_{\text{inc}}^{(\text{H})}$
$b_{\alpha\beta}^{(fi)}$ Singlet-Singlet			
$\alpha = 1$	$\sigma_{\text{coh}}^{(\text{Si})}$	$-\sqrt{\sigma_{\text{coh}}^{(\text{Si})} \cdot \sigma_{\text{coh}}^{(\text{H})}}$	$-\sqrt{\sigma_{\text{coh}}^{(\text{Si})} \cdot \sigma_{\text{coh}}^{(\text{H})}}$
$\alpha = 2$	$-\sqrt{\sigma_{\text{coh}}^{(\text{Si})} \cdot \sigma_{\text{coh}}^{(\text{H})}}$	$\sigma_{\text{coh}}^{(\text{H})}$	$\sigma_{\text{coh}}^{(\text{H})}$
$\alpha = 3$	$-\sqrt{\sigma_{\text{coh}}^{(\text{Si})} \cdot \sigma_{\text{coh}}^{(\text{H})}}$	$\sigma_{\text{coh}}^{(\text{H})}$	$\sigma_{\text{coh}}^{(\text{H})}$
$b_{\alpha\beta}^{(fi)}$ Distinguishable			
$\alpha = 1$	$\sigma_{\text{scatt}}^{(\text{Si})}$	$-\sqrt{\sigma_{\text{coh}}^{(\text{Si})} \cdot \sigma_{\text{coh}}^{(\text{H})}}$	$\sqrt{\sigma_{\text{coh}}^{(\text{Si})} \cdot \sigma_{\text{coh}}^{(\text{D})}}$
$\alpha = 2$	$-\sqrt{\sigma_{\text{coh}}^{(\text{Si})} \cdot \sigma_{\text{coh}}^{(\text{H})}}$	$\sigma_{\text{scatt}}^{(\text{H})}$	$-\sqrt{\sigma_{\text{coh}}^{(\text{H})} \cdot \sigma_{\text{coh}}^{(\text{D})}}$
$\alpha = 3$	$\sqrt{\sigma_{\text{coh}}^{(\text{Si})} \cdot \sigma_{\text{coh}}^{(\text{D})}}$	$-\sqrt{\sigma_{\text{coh}}^{(\text{H})} \cdot \sigma_{\text{coh}}^{(\text{D})}}$	$\sigma_{\text{scatt}}^{(\text{D})}$

compared with the diagonal coefficient ($\sigma_{\text{coh}}^{(\text{H})}/\sigma_{\text{scatt}}^{(\text{H})} \approx 1/40$ [41]).

The disappearance of the $S(Q)$ in the 2SC level [226 meV, blue circles in Fig. 2(c)] is due to the symmetry of the wave function. Because the spin state of the 2SC level is singlet ($n_{3\rho} = n_{\text{even}}$), scattering occurs from the singlet ground states to the singlet excited states. The scattering does not change the neutron spin and is characterized by the coherent scattering cross section, therefore the spectrum disappeared in the 2SC level ($\sigma_{\text{coh}}^{(\text{H})}/\sigma_{\text{scatt}}^{(\text{H})} \approx 1/40$ [41]). To reproduce the theoretical $S(Q)$ in the 2SC level, we utilized the $b_{\alpha\beta}^{(fi)}$ denoted in Table I, singlet to singlet. The discrepancy between the experimental plots (blue circles) and the theoretical curve (blue line) originates for the following reasons: (a) the existence of the background scattering components from the other energy levels, such as 3M and 3N bending modes, (b) the relaxation of spin orthogonality, and/or (c) the existence of anharmonicity due to the interaction between the surrounding protons. It is likely that the weak infrared absorbance of the SiH bending mode compared to the strong absorbance of the SiH bending mode (the ratio of absorbance is approximately 10^{-4} [33,50,51]) originates from the above (b) and/or (c) reasons. For comparison, the theoretical $S(Q, \hbar\omega = 226 \text{ meV})$ without the effects from entanglement is plotted as the dotted blue line in Fig. 2(c). [The coefficient $b_{\alpha\beta}^{(fi)}$ was selected based on Table I, distinguishable case, where we replace $\sigma_{\text{scatt}}^{(\text{D})}$ to $\sigma_{\text{scatt}}^{(\text{H})}$ and $(\sigma_{\text{coh}}^{(\text{D})})^{1/2}$ to $-(\sigma_{\text{coh}}^{(\text{H})})^{1/2}$.] Had the effects from entanglement not been present, the 2SC level would have exhibited a strong incoherent scattering spectrum.

When the antisymmetry for the exchange of the coordinates of the two proton particles is broken, and this condition is fulfilled using the deuteron substitution, the theoretically calculated lines [red and blue dotted lines in

Fig. 3(c)] clearly reproduce the disappearance of the antisymmetry. The experimental results demonstrate that the intense scattering behaviors of both the 1DSC and 2DSC levels, shown in Fig. 3(c), and the disappearance of the interference in the 1DSC level, shown in the FT spectra (red circles: experiment, blue line: theoretical curve) of Fig. 3(d), are theoretically confirmed as stemming from the loss of the entanglement. Thus the disappearance of the antisymmetry due to deuteron substitution provides further confirmation that the two proton particles are in a quantum entangled state. Here, the calculation of $S(Q)$ for both the 1DSC and 2DSC levels was based on the $b_{\alpha\beta}^{(fi)}$ in Table I, distinguishable case [42–44]. The calculated energy levels for the first excited states are summarized in the inset of Fig. 3(d), where $E(n_{1X} + n_{1Y} = 1) = 52 \text{ meV}$, $E(n_{1Z} = 1) = 58 \text{ meV}$, $E(n_{2X} + n_{2Y} = 1) = 72 \text{ meV}$, $E(n_{3X} + n_{3Y} = 1) = 97 \text{ meV}$, $E(n_{2Z} = 1) = 192 \text{ meV}$, and $E(n_{3Z} = 1) = 267 \text{ meV}$.

IV. DISCUSSION

At a glance, both symmetric and antisymmetric states are present in each scissor vibrational state, and both spin singlet and triplet states seem to be mixed. These phenomena are known as inversion doubling of light molecules due to the internal spatial inversion of their nuclear conformations by tunneling [52–55]. However, in our case, the spatial inversion hardly occurs due to the rigid bonding of SiH₂ to the crystalline Si surface, and the parity of the normal modes are clearly separated. For example, the symmetrical or antisymmetrical vibrational states can be correlated to the spin states as $|\Psi_S\rangle = |\Phi_S\rangle|0\rangle_1|1\rangle_{\text{Singlet}}_{2,3}$ or $|\Psi_A\rangle = |\Phi_A\rangle|0\rangle_1|1\rangle_{\text{Triplet}}_{2,3}$ where $|\Phi_S\rangle = 1/\sqrt{2}(|1, 2, 3\rangle + |1, 3, 2\rangle)$ and $|\Phi_A\rangle =$

$1/\sqrt{2}(|1, 2, 3\rangle - |1, 3, 2\rangle)$ (1: Si, 2: H, 3: H) [42,43,52–55], and the doublet is assumed to be degenerated. However, when we transform these vibrational states to the eigenstates, these states can be described by using the normal coordinates ξ_1, ξ_2, ξ_3 and the quantum number n as $\Phi_S(n; \xi_1, \xi_2, \xi_3) = 1/\sqrt{2}(\langle n; \xi_1, \xi_2, \xi_3 | 1, 2, 3\rangle + \langle n; \xi_1, \xi_2, \xi_3 | 1, 3, 2\rangle)$, or $\Phi_A(n; \xi_1, \xi_2, \xi_3) = 1/\sqrt{2}(\langle n; \xi_1, \xi_2, \xi_3 | 1, 2, 3\rangle - \langle n; \xi_1, \xi_2, \xi_3 | 1, 3, 2\rangle)$. We note here that the $\langle n; \xi_1, \xi_2, \xi_3 | 1, 2, 3\rangle$ is described by the Hermit functions, so the parity is clearly separated. For example, when $n_{3\rho} = n_{\text{odd}}$ energy levels (odd number SC modes), $\langle n; \xi_1, \xi_2, \xi_3 | 1, 2, 3\rangle = -\langle n; \xi_1, \xi_2, \xi_3 | 1, 3, 2\rangle$, $\Psi_S(n; \xi_1, \xi_2, \xi_3)$ disappeared and only triplet states exist in these states. On the other hand, all the other energy levels except $n_{3\rho} = n_{\text{odd}}$, such as $n = n_{1\rho}, n_{2\rho}$, and $n_{3\rho} = n_{\text{even}}$ energy levels, $\langle n; \xi_1, \xi_2, \xi_3 | 1, 2, 3\rangle = \langle n; \xi_1, \xi_2, \xi_3 | 1, 3, 2\rangle$, and $\Psi_A(n; \xi_1, \xi_2, \xi_3)$ disappeared. Only singlet states are observed in these states. Therefore, the mixture of the spin states does not occur, and the vibrational modes of the X, Y direction are clearly separated as the two singlet states (58 and 82 meV) and the one triplet state (113 meV) as shown in the inset of Fig. 2(d). On the other hand, for the modes of the Z direction, the energy separation between the singlet state (265 meV) and the triplet state (269 meV) is small; therefore, the symmetric and antisymmetric states of the Z direction are observed as one state by INS measurements. All the energies, the spin states, and the possible transition types are denoted in the inset of Fig. 2(d).

The obtained quantum entangled states (both the singlet states and triplet states) can be used to generate a cascade transition of entangled THz photon pairs through the magnetic dipole interaction, because the experimentally determined energy levels and the spin states correspond to a pair of spin half particles confined together in a harmonic potential [56–58]. For example, evenly spaced energy ladders with the singlet spin states for n_{even} energy levels and the triplet spin states for n_{odd} energy levels are ideal sources of the cascade transition of THz entangled photons (27 THz), as shown in Fig. 1(c). In this case, the entangled photon states $|\Theta_{20}\rangle$ from $n = 2$ to $n = 0$ become $|\Theta_{20}\rangle = 1/\sqrt{2}(|L_{21}\rangle|L_{10}\rangle + |R_{21}\rangle|R_{10}\rangle)$, where $|R_{m-1}\rangle$ and $|L_{m-1}\rangle$ denote the transition from the n to $n - 1$ energy level with the right and left circulation polarization, respectively. Additionally, by exciting the SC mode to the higher energy $2n$ level, the cascade transitions of the entangled photon pairs $|\Theta_{2n0}\rangle$ can be created as follows: $|\Theta_{2n0}\rangle = \bigotimes_{j=1}^n |\Theta_{2j2j-2}\rangle$, where the photons have the same energy. We note here that the transition from the singlet state to the triplet state is forbidden by the spin orthogonality. In this case, the excitation might be performed by using an electron beam or two photon absorption process. By constructing a THz cavity whose operation principle is similar to that of the hydrogen maser (magnetic dipole interaction) [45–47], we consider that

it is possible to obtain strong induced emission of the entangled THz photons. The possibility of the qubits that demand the DiVincenzo criteria [59] are now under experimental investigation by measuring the longitudinal (T_1) and transverse (T_2) relaxation times for both the 1SC and 2SC states.

V. CONCLUSION

In conclusion, the results obtained by the INS measurements provide direct evidence that the vibrational and proton spin wave functions are correlated, and strongly entangled states are formed for all the energy levels of infrared vibrations. This entanglement is characterized by an enormous energy difference of 113 meV between the spin singlet ground state and the spin triplet excited state. We theoretically demonstrated the cascade transition of THz entangled photon pairs utilizing proton entanglement. These results of entanglement states are obtained from the Si(100) 1×1 surface. However, we consider that other types of semiconductor surfaces such as C(100) 1×1 and Ge(100) 1×1 are also possible candidates for the proton entanglements.

By using polarized neutrons, it is possible to distinguish the different excitation process for the 1SC and 2SC mode more precisely because, according to our analysis, the excitation of 1SC should be a spin flip excitation, while the 2SC excitation corresponds to a non-spin-flip process. Furthermore, the 1SC mode is triply degenerated; this degeneracy can be resolved by using a neutron spectrometer with a much higher resolution through the application of a magnetic field. The spin polarized neutron scattering experiments, the resolution of triply degenerated states, as well as the temperature dependence of the interference property will provide additional information pertaining to the physical properties of the 1SC mode. These topics are currently under investigation and they will be reported in a subsequent study.

The qubits proposed here, which are composed of a pair of spin half particles in a harmonic potential, have similar physical nature as the established qubits composed of photons or atoms. We believe that the combination of the entangled proton qubits and sophisticated Si technologies could offer a useful platform for information, communication, and computation technologies.

ACKNOWLEDGMENTS

We thank Prof. D. Hanawa for helping with our numerical simulation. T.M. thanks Prof. H. Kusama for fruitful discussions. T.O. and S.I. thank Prof. S. M. Bennington for assistance with the inelastic neutron scattering measurements. This work was financially supported by JSPS KAKENHI Grant No. 20H04455.

[1] R. Horodecki, P. Horodecki, M. Horodecki, and K. Horodecki, Quantum entanglement, *Rev. Mod. Phys.* **81**, 865 (2009).
 [2] J. Audretsch, *Entangled Systems: New Directions in Quantum Physics* (Wiley-VCH, Weinheim, 2007).
 [3] A. Zeilinger, Light for the quantum. Entangled photons and their applications: A very personal, *Phys. Scr.* **92**, 072501 (2017).

[4] G. Falci, R. Fazio, G. M. Palma, J. Siewert, and V. Vedral, Detection of geometric phases in superconducting nanocircuits, *Nature (London)* **407**, 355 (2000).
 [5] A. A. Abdumalikov Jr., J. M. Fink, K. Juliusson, M. Pechal, S. Berger, A. Wallraff, and S. Filipp, Experimental realization of non-Abelian non-adiabatic geometric gates, *Nature (London)* **496**, 482 (2013).

- [6] J. Clarke and F. K. Wilhelm, Superconducting quantum bits, *Nature (London)* **453**, 1031 (2008).
- [7] I. Chiorescu, Y. Nakamura, C. J. P. M. Harmans, and J. E. Mooij, Coherent quantum dynamics of a superconducting flux qubit, *Science* **299**, 1869 (2003).
- [8] D. Kielpinski, C. Monroe, and D. J. Wineland, Architecture for a large-scale ion-trap quantum computer, *Nature (London)* **417**, 709 (2002).
- [9] R. Blatt and D. J. Wineland, Entangled states of trapped atomic ions, *Nature (London)* **453**, 1008 (2008).
- [10] S. Debnath, N. M. Linke, C. Figgatt, K. A. Landsman, K. Wright, and C. Monroe, Demonstration of a small programmable quantum computer with atomic qubits, *Nature (London)* **536**, 63 (2016).
- [11] C. Figgatt, A. Ostrander, N. M. Linke, K. A. Landsman, D. Zhu, D. Maslov, and C. Monroe, Parallel entangling operations on a universal ion-trap quantum computer, *Nature (London)* **572**, 368 (2019).
- [12] W. Huang, C. H. Yang, K. W. Chan, T. Tanttu, B. Hensen, R. C. C. Leon, M. A. Fogarty, J. C. C. Hwang, F. E. Hudson, K. M. Itoh, A. Morello, A. Laucht, and A. S. Dzurak, A silicon quantum-dot-coupled nuclear spin qubit, *Nature (London)* **569**, 532 (2019).
- [13] Y. He, S. K. Gorman, D. Keith, L. Kranz, J. G. Keizer, and M. Y. Simmons, A two-qubit gate between phosphorus donor electrons in silicon, *Nature (London)* **571**, 371 (2009).
- [14] L. Petit, H. G. J. Eenink, M. Russ, W. I. L. Lawrie, N. W. Hendrickx, S. G. J. Philips, J. S. Clarke, L. M. K. Vandersypen, and M. Veldhorst, Universal quantum logic in hot silicon qubits, *Nature (London)* **580**, 355 (2020).
- [15] C. H. Yang, R. C. C. Leon, J. C. C. Hwang, A. Saraiva, T. Tanttu, W. Huang, J. Camirand Lemyre, K. W. Chan, K. Y. Tan, F. E. Hudson, K. M. Itoh, A. Morello, M. Pioro-Ladrière, A. Laucht, and A. S. Dzurak, Operation of a silicon quantum processor unit cell above one kelvin, *Nature (London)* **580**, 350 (2020).
- [16] A. Gaita-Ariño, F. Luis, S. Hill, and E. Coronado, Molecular spins for quantum computation, *Nat. Chem.* **11**, 301 (2019).
- [17] P. Rabl, D. DeMille, J. M. Doyle, M. D. Lukin, R. J. Schoelkopf, and P. Zoller, Hybrid Quantum Processors: Molecular Ensembles as Quantum Memory for Solid State Circuits, *Phys. Rev. Lett.* **97**, 033003 (2006).
- [18] G. Feng, G. Xu, and G. Long, Experimental Realization of Nonadiabatic Holonomic Quantum Computation, *Phys. Rev. Lett.* **110**, 190501 (2013).
- [19] G. D. Fuchs, G. Burkard, P. V. Klimov, and D. D. Awschalom, A quantum memory intrinsic to single nitrogen–vacancy centres in diamond, *Nat. Phys.* **7**, 789 (2011).
- [20] A. Gruber, A. Dräbenstedt, C. Tietz, L. Fleury, J. Wrachtrup, and C. von Borczyskowski, Scanning confocal optical microscopy and magnetic resonance on single defect centers, *Science* **276**, 2012 (1997).
- [21] M. W. Doherty, N. B. Manson, P. Delaney, F. Jelezko, J. Wrachtrup, and L. C. L. Hollenberg, The nitrogen-vacancy colour centre in diamond, *Phys. Rep.* **528**, 1 (2013).
- [22] M. D. LaHaye, O. Buu, B. Camarota, and K. C. Shwab, Approaching the quantum limit of a nanomechanical resonator, *Science* **304**, 74 (2004).
- [23] M. D. LaHaye, J. Suh, P. M. Echternach, K. C. Shwab, and M. L. Roukes, Nanomechanical measurements of a superconducting qubit, *Nature (London)* **459**, 960 (2009).
- [24] S. Barzanjeh, E. S. Redchenko, M. Peruzzo, M. Wulf, D. P. Lewis, G. Arnold, and J. M. Fink, Stationary entangled radiation from micromechanical motion, *Nature (London)* **570**, 480 (2019).
- [25] A. Ajoy, U. Bissbort, M. D. Lukin, R. L. Walsworth, and P. Cappellaro, Atomic-Scale Nuclear Spin Imaging using Quantum-Assisted Sensors in Diamond, *Phys. Rev. X* **5**, 011001 (2015).
- [26] L. T. Hall, G. C. G. Beart, E. A. Thomas, D. A. Simpson, L. P. McGuinness, J. H. Cole, J. H. Manton, R. E. Scholten, F. Jelezko, J. Wrachtrup, S. Petrou, and L. C. Hollenberg, High spatial and temporal resolution wide-field imaging of neuron activity using quantum NV-diamond, *Sci. Rep.* **2**, 401 (2012).
- [27] S. Baumann, W. Paul, T. Choi, C. P. Lutz, A. Ardavan, and A. J. Heinrich, Electron paramagnetic resonance of individual atoms on a surface, *Science* **350**, 417 (2015).
- [28] Y.-J. Lin, I. Teper, C. Chin, and V. Vuletić, Impact of the Casimir-Polder Potential and Johnson Noise on Bose-Einstein Condensate Stability near Surfaces, *Phys. Rev. Lett.* **92**, 050404 (2004).
- [29] B. A. Myers, A. Das, M. C. Dartiailh, K. Ohno, D. D. Awschalom, and A. C. Bleszynski Jayich, Probing Surface Noise with Depth-Calibrated Spins in Diamond, *Phys. Rev. Lett.* **113**, 027602 (2014).
- [30] D. M. Dennison, A note on the specific heat of the hydrogen molecule, *Proc. R. Soc. London, Ser. A* **115**, 483 (1927).
- [31] *Atkins' Physical Chemistry*, 8th ed., edited by P. Atkins and J. de Paula (Freeman, New York, 2006).
- [32] L. T. Canham, Silicon quantum wire array fabrication by electrochemical and chemical dissolution of wafers, *Appl. Phys. Lett.* **57**, 1046 (1990).
- [33] T. Matsumoto, A. I. Belogorokhov, L. I. Belogorokhova, Y. Masumoto, and E. A. Zhukov, The effect of deuterium on the optical properties of free-standing porous silicon layers, *Nanotechnology* **11**, 340 (2000).
- [34] T. Matsumoto, J. Suzuki, M. Ohnuma, Y. Kanemitsu, and Y. Masumoto, Evidence of quantum size effect in nanocrystalline silicon by optical absorption, *Phys. Rev. B* **63**, 195322 (2001).
- [35] Y. Kanemitsu, H. Uto, Y. Masumoto, T. Matsumoto, T. Futagi, and H. Mimura, Microstructure and optical properties of free-standing porous silicon films: Size dependence of absorption spectra in Si nanometer-sized crystallites, *Phys. Rev. B* **48**, 2827 (1993).
- [36] A. G. Cullis, L. T. Canham, and P. D. J. Calcott, The structural and luminescence properties of porous silicon, *J. Appl. Phys.* **82**, 909 (1997).
- [37] *Handbook of Porous Silicon*, edited by L. T. Canham (Springer, Cham, Switzerland, 2014).
- [38] T. Matsumoto, T. Ohhara, H. Sugimoto, S. M. Bennington, and S. Ikeda, Quantum twin spectra in nanocrystalline silicon, *Phys. Rev. Materials* **1**, 051601(R) (2017).
- [39] Y. J. Chabal, G. S. Higashi, and K. Raghavachari, Infrared spectroscopy of Si (111) and Si (100) surfaces after HF treatment: Hydrogen termination and surface morphology, *J. Vac. Sci. Technol. A* **7**, 2104 (1989).
- [40] J. E. Northrup, Structure of Si(100)H: Dependence on the H chemical potential, *Phys. Rev. B* **44**, 1419(R) (1991).
- [41] A. J. Dianoux and G. Lander, *Neutron Data Booklet* (Institut Laue-Langevin, Grenoble, France, 2003).

- [42] H. Sugimoto, H. Yuuki, and A. Okumura, Effects of Entanglement on the Scattering Intensity of Neutron Compton Scattering by a Proton Pair in Solids, *Phys. Rev. Lett.* **94**, 165506 (2005).
- [43] H. Sugimoto, A. Okumura, and H. Yuuki, Effects of entanglement on elastic and inelastic scattering functions for neutron scattering from a pair of nuclei in solids, *Phys. Rev. B* **73**, 014305 (2006).
- [44] E. B. Karlsson and S. W. Lovesey, Neutron Compton scattering by proton and deuteron systems with entangled spatial and spin degrees of freedom, *Phys. Rev. A* **61**, 062714 (2000).
- [45] D. Kleppner, H. M. Goldenberg, and N. F. Ramsey, Theory of the hydrogen maser, *Phys. Rev.* **126**, 603 (1962).
- [46] N. F. Ramsey, The atomic hydrogen maser, *Metrologia* **1**, 7 (1965).
- [47] W. Happer, Optical pumping, *Rev. Mod. Phys.* **44**, 169 (1972).
- [48] S. Ikeda, S. Kashida, H. Sugimoto, Y. Yamada, S. M. Bennington, and F. Fillaux, Inelastic neutron scattering study of the localized dynamics of protons in KHCO_3 single crystals, *Phys. Rev. B* **66**, 184302 (2002).
- [49] S. Ikeda, M. Furusaka, T. Fukunaga, and A. D. Taylor, Hydrogen wave functions in the metal hydrides ZrH_2 and $\text{NbH}_{0.3}$, *J. Phys.: Condens. Matter* **2**, 4675 (1990).
- [50] D. J. Michalak, S. R. Amy, D. Aureau, M. Dai, A. Estève, and Y. J. Chabal, Nanopatterning Si(111) surfaces as a selective surface-chemistry route, *Nat. Mater.* **9**, 266 (2010).
- [51] A. A. Langford, M. L. Fleet, B. P. Nelson, W. A. Lanford, and N. Maley, Infrared absorption strength and hydrogen content of hydrogenated amorphous silicon, *Phys. Rev. B* **45**, 13367 (1992).
- [52] H.-H. Limbach, G. Buntkowsky, J. Matthes, S. Grndemann, T. Pery, B. Walaszek, and B. Chaudret, Novel insights into the mechanism of the ortho/para spin conversion of hydrogen pairs: Implications for catalysis and interstellar water, *Chem. Phys. Chem.* **7**, 551 (2006).
- [53] I. F. Silvera, The solid molecular hydrogens in the condensed phase: Fundamental and static properties, *Rev. Mod. Phys.* **52**, 393 (1980).
- [54] A. Miani and J. Tennyson, Can ortho–para transitions for water be observed? *J. Chem. Phys.* **120**, 2732 (2004).
- [55] I. Gonzalo and M. A. Antón, Entangling non planar molecules via inversion doublet transition with negligible spontaneous emission, *Phys. Chem. Chem. Phys.* **21**, 10523 (2019).
- [56] K. Mølmer and A. Sørensen, Multiparticle Entanglement of Hot Trapped Ions, *Phys. Rev. Lett.* **82**, 1835 (1999).
- [57] K. Edamatsu, G. Oohata, R. Shimizu, and T. Itoh, Generation of ultraviolet entangled photons in a semiconductor, *Nature (London)* **431**, 167 (2004).
- [58] G. Oohata, R. Shimizu, and K. Edamatsu, Photon Polarization Entanglement Induced by Biexciton: Experimental Evidence for Violation of Bell’s Inequality, *Phys. Rev. Lett.* **98**, 140503 (2007).
- [59] D. P. DiVincenzo, The physical implementation of quantum computation, *Fortschr. Phys.* **48**, 771 (2000).